

A Theoretical Perspective to Decipher the Origin of High Hydrogen Storage Capacity in Mn(II) Metal-Organic Framework

Reshma Jose,^[a] Sourav Pal,^{*[b, c]} and Gopalan Rajaraman^{*[a]}

Herein, we report a detailed periodic DFT investigation of Mn(II)-based $[(\text{Mn}_4\text{Cl})_3(\text{BTT})_8]^{3-}$ ($\text{BTT}^{3-} = 1,3,5\text{-benzenetristetrazolate}$) metal-organic framework (MOF) to explore various hydrogen binding pockets, nature of MOF...H₂ interactions, magnetic coupling and, H₂ uptake capacity. Earlier experiments found an uptake capacity of 6.9 wt % of H₂ with the heat of adsorption estimated to be ~10 kJ/mol, which is one among the highest for any MOFs reported. Our calculations unveil different binding sites with computed binding energy varying from -6 to -15 kJ/mol. The binding of H₂ at the Mn²⁺ site is found to be the strongest (site I), with H₂ found to bind Mn²⁺ ion in a η^2 fashion with a distance of 2.27 Å and binding energy of -15.4 kJ/mol. The bonding analysis performed using NBO and AIM reveal a strong donation of σ (H₂) to the d_{z^2} orbital of the Mn²⁺ ion responsible for such large binding energy. The other binding pockets, such as -Cl (site II) and BTT ligands (site III and IV) were found to be weaker, with the binding energy decreasing in the order I > II > III > IV. The average binding energy computed for these four sites put together is 9.6 kJ/mol, which is in excellent agreement with the experimental value of

~10 kJ/mol. We have expanded our calculations to compute binding energy for multiple sites simultaneously, and in this model, the binding energy per site was found to decrease as we increased the number of H₂ molecules suggesting electronic and steric factors controlling the overall uptake capacity. The calculated adsorption isotherm using the GCMC method reproduces the experimental observations. Further, the magnetic coupling computed for the unbound MOF reveals moderate ferromagnetic and strong antiferromagnetic coupling within the tetrameric {Mn₄} unit leading to a three-up-one-down spin configuration as the ground state. These were then coupled ferromagnetically to other tetrameric units in the MOF network. The magnetic coupling was found to alter only marginally upon gas binding, suggesting that both exchange interaction and the spin-states are unlikely to play a role in the H₂ uptake. This is contrary to the O₂ uptake studied lately, where strong dependence on exchange-coupling/spin state was witnessed, suggesting exchange-coupling/magnetic field dependent binding as a viable route for gas separation.

Introduction

The development of a safe and effective gas storage system is crucial for implementing fuel cell economy. Although many strategies have emerged to improve the efficiency of the gas storage system, Metal-Organic Frameworks (MOFs) based storage systems have attracted wide interest. MOFs consist of central metal atoms that are connected by organic linkers and

extend in three-dimensional space to form a porous coordination network. MOFs possess remarkable features such as large surface area, tunable porosity, diversity in metal functional groups, structural and chemical tunability, which has grabbed the interest of today's research community and opened a new window for various applications in the field of heterogeneous catalysis^[1-5] sensing,^[6-10] drug delivery,^[11-17] gas adsorption^[18-28] and storage^[29-39] etc.^[40-42] The metal center possesses unique properties like size extensivity, functionality, and the linking of the organic moiety to the metal part, providing architecturally robust and more crystalline MOF with extensive porosity that exceeds that of porous materials such as zeolites and COFs.^[43] Unlike zeolites and other porous materials, there exists fascinating chemistry between coordinating linker molecules and the geometry of the metal center in MOFs.^[44] The large thermal stability of these MOFs made them amenable to various functionalisation and modification.^[45] The MOF can serve as a platform for numerous applications due to their flexibility with which they possess fascinating structural as well as chemical properties, which allow the incorporation of new entities in a diverse manner.

A majority of the MOFs reported in the literature contain paramagnetic metal ions, which offer additional electronic flexibility and spin-coupling, aiding improved binding of guests

- [a] R. Jose, Prof. G. Rajaraman
Department of Chemistry,
Indian Institute of Technology Bombay,
Powai, Mumbai-400076, India
E-mail: rajaraman@chem.iitb.ac.in
Homepage: <https://www.chem.iitb.ac.in/~rajaraman/>
- [b] Prof. S. Pal
Department of Chemistry
Indian Institute of Science Education and Research,
Kolkata, Mohanpur, Nadia – 741246, India
- [c] Prof. S. Pal
Department of Chemistry, Ashoka University, Sonapat,
Haryana 131029, India
E-mail: sourav.pal@ashoka.edu.in

Supporting information for this article is available on the WWW under <https://doi.org/10.1002/cphc.202200257>

An invited contribution to the Special Collection featuring the Theoretical Chemistry Symposium 2021

and could provide clues on the cooperative binding of the guest molecule to the framework. The cooperative properties exhibited by MOFs, such as magnetic ordering and spin crossover, affirm this point. Hence, controlling the magnetic properties of MOFs by incorporating various functionalities and paramagnetic centers and thereby tuning their gas binding properties are crucial for the molecular design of paramagnetic MOFs. In light of this, we were interested in tuning the magnetic properties of MOFs through density functional theory-based modelling studies. The series of M-BTT frameworks ($\text{BTT}^{3-} = 1,3,5\text{-benzenetristetrazolate}$) where $M = \text{Cr, Mn, Fe, Co, Ni, Cu, Cd}$ are promising candidates for the binding of various gases such as hydrogen, carbon monoxide, oxygen, etc., and various experimental pieces of evidence prove their unique binding affinities.^[18,20,46–48] Thus, the modification of the chemical environment by keeping the structural features the same^[49], the M-BTT family can act as a platform for the excellent adsorption of the various gases. Notably, Dinca et al. reported $[\text{Mn}(\text{DMF})_6]_3[(\text{Mn}_4\text{Cl})_3(\text{BTT})_8(\text{H}_2\text{O})_{12}]_2$ in rare cubic topology, which shows uptake of H_2 up to 6.9 wt % at 77 k and 90 bar^[50] which is closer to the latest DOE target for the deliverable capacity of 8 wt % and 52 g/L. Further, this MOF exhibits isosteric heat of adsorption of 10.1 kJ/mol, one of the highest known to date. This unusually large uptake of H_2 is puzzling, and the presence of open metal sites alone can not account for such large uptake hence in light of this, here we have chosen the Mn-BTT framework for the periodic DFT (Density Functional Theory) based investigations to answer the following specific questions (i) how many binding sites are there in this MOF and what are their binding energy (ii) what is the nature of MOF... H_2 interactions?^[51–55] (iii) is the magnetic exchange between the metal-centers altered upon H_2 binding? (iv) is there any cooperative binding among different pockets in H_2 uptake?^[56]

Computational Details

All calculations and geometry optimisation were carried out using CP2k software using periodic boundary conditions.^[57,58] The TPSS exchange-correlation functional along with DFT–D2 corrections were used for the calculations of binding energy as well as single point energy.^[59–61] The basis set chosen for Mn, C, H, N, Cl was DZVP- MOLOPT- GTH, with a gaussian plane wave (GPW) approach. A kinetic energy cut-off of 400 Ry was applied for the calculations and BFGS optimisation routines. The cell parameters were obtained by extending the unit cell in three-dimensional space using the X-ray structure reported. The $a=b=c=19.1158 \text{ \AA}$ was giving the proper repeating unit by following the periodic boundary conditions. We have employed polarised spin calculations to account for the hydrogen bonding interaction with respect to different spin states. We have computed the energy of various spin states, such as high spin and all other broken symmetries, and obtained the exchange coupling interaction in order to understand the nature of the spin coupling in the ground state.^[62] The Noodleman's broken symmetry approach was used for the estimation of exchange values. The estimation of the J value also gave the possibility to understand the energy level structure of spin states.^[63,64] The J values were estimated using TPSS functional and to check the validity of the employed method, a limited benchmarking employing BLYP, Beck88 and PBE functionals was performed (See Table S1) in ESI. While there are minor variations in the J_1 , all the functionals

predict that J_2 is the strongest interaction and is antiferromagnetic in nature, yielding the same ground state. Similarly, the J_3 interaction is also found to be ferromagnetic, with a minor variation in the magnitude noted. The J_1 interaction being very small was found to vary, with two of the functionals predicting it to be weakly antiferromagnetic in nature.

The partial and total density of states was computed to understand the interaction of various d-orbitals with H_2 molecules. Further calculations such as NBO (Natural Bond Orbital) and estimation of the energy of the small model system were performed using G09 software, and AIM (Atoms in Molecules) analysis was performed using Multiwfn software.^[93] Several DFT, coupled-cluster and symmetry-adapted perturbation theory-based studies^[65,66] are available in the literature exploring various aspects related to H_2 binding and uptake in MOFs.^[67–69] The research frontier for hydrogen storage currently is how to store hydrogen at room temperature with a pressure swing. As some of the binding site estimated here are purely dispersive type interactions, we have checked the corresponding binding energy for a possible basis set superposition errors, and the counterpoise correction performed for one of the sites reveal a minimum deviation ($\sim 0.7 \text{ kJ/mol}$, see ESI for further details). Additionally, all the sites identified here have strong support from experiments in terms of the neutron diffraction data. Further, to check the validity of the dispersive correction employed in our DFT calculations, we have performed DLPNO-CCSD(T)/cc-pVTZ calculations on a cluster model optimised within the DFT framework. For the site IV model, the DLPNO-CCSD(T) yields binding energy of -4.2 kJ/mol , while DFT calculations yield a relatively higher estimate (-6.4 kJ/mol , vide infra), and this suggests a potential error bar of $\sim 30\%$, and this could be due to insufficient dispersion correction in the DFT methods employed. Further details on these calculations and the model employed are given in ESI (Figure S4).

Recent computational studies predicted up to 7 wt % and 24 g/L deliverable capacities for some MOFs with a wider range of temperatures and pressures, and their wt % is comparable to the Mn-MOF studied here.^[70] The adsorption isotherm simulations were performed through the Grand Canonical Monte Carlo technique as implemented in the RASPA software.^[71] The Generic MOF force field^[72,73] parameters were considered to incorporate the Lennard-Jones (LJ) parameters for the framework atoms, and Lorentz-Berthelot mixing rules are used to calculate the cross interactions. The H_2 molecules were modelled using the TraPPE force field, and this has been used earlier for modelling H_2 adsorption isotherms, though the force field parameters were not specifically tuned for this particular system.^[74–77] We performed each simulation with 50,000 equilibration cycles and 50,000 production cycles and considered insertion, deletion, translation, and rotation moves. The supercell for simulation was created using the Molden software. There are several literature reports on Force field-based GCMC calculations for obtaining the adsorption isotherm for H_2 ,^[78] which predict that the storage capacity is strongly correlated with the MOF pore volume than with the MOF surface area.^[79]

Results and Discussion

For our calculations, we have chosen the $[(\text{Mn}_4\text{Cl})_3(\text{BTT})_8]^{3-}$ as our model from the crystallographic information available in the database.^[46] The chosen unit cell contains three tetrameric units of manganese ions connected through chloride bridges, and the nearby manganese centers are connected through the tetrazolate bridge of the BTT^{3-} (Benzene Tris Tetrazolate)

ligand.^[46] This structure was optimised using periodic boundary conditions, and the optimised structure of unbound MOF's repeating unit is shown in Figure 1(a). The computed Mn–Mn, Mn–N, and Mn–Cl distances, Mn–Cl–Mn angle are 3.67 Å, 2.18 Å and 2.58 Å, 90°, which is in agreement with the X-ray structure reported (average Mn–Mn distance 3.86 Å, Mn–N distance is 2.27 Å, Mn–Cl distance is 2.73 Å and Mn–Cl–Mn angle 90°). Further periodic DFT calculations were performed with a neutral unit cell with a formula of $[(\text{Mn}_4\text{Cl})_3(\text{BTT})_5(\text{BTTH})_3]$ by adding protons to the non-coordinated nitrogen atoms of the triazolate group, as suggested earlier.^[80] This model yields binding energy (−13.4 kJ/mol), and this is similar to the other models that were attempted here (−15 kJ/mol).

Hydrogen Binding by the Mn-BTT MOF

The experimental pieces of evidence suggest that the initial framework was formulated as $[(\text{Mn}_4\text{Cl})_3(\text{BTT})_8(\text{H}_2\text{O})_{12}]^{3-}$ where water ligands occupy the sixth coordination site on each Mn^{2+} ion, while charge balance is provided by $[\text{Mn}(\text{DMF})_6]^{2+}$ complexes situated inside the sodalite cage-like units. The $[\text{Mn}(\text{DMF})_6]^{2+}$ unit perfectly fits the large cavity formed by the eight BTT ligands. Further thermogravimetric analysis of the framework suggested that the majority of the cationic sites were occupied by DMF, which was hindering the availability of the unsaturated Mn^{2+} sites and causing the reduction of the available surface area. The exchange of DMF with methanol was carried out in order to remove the DMF solvent and complete the evacuation process, which resulted in a framework free of water and methanol with more available coordination sites for gases. Based on these experimental findings $[(\text{Mn}_4\text{Cl})_3(\text{BTT})_8]^{3-}$

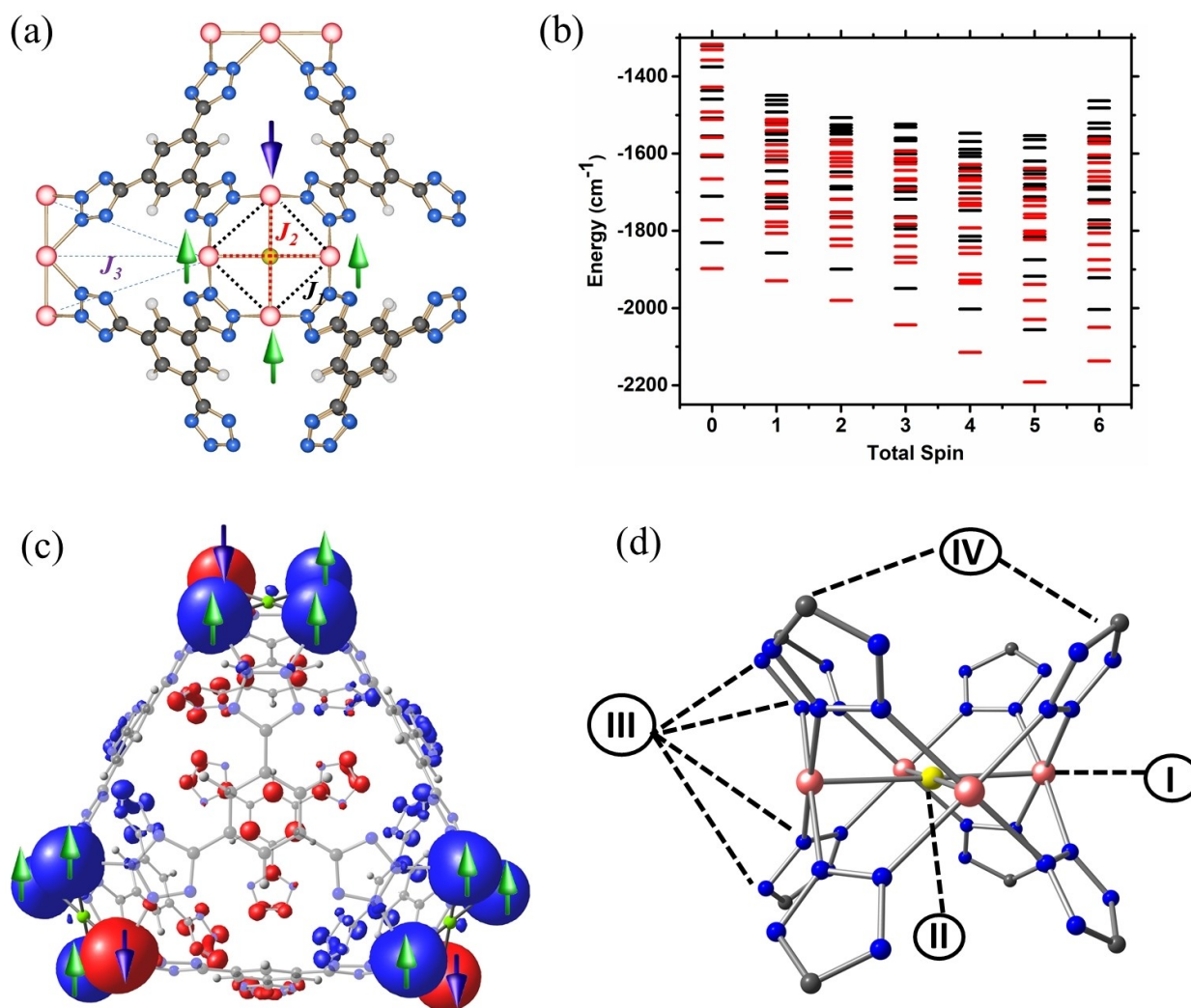


Figure 1. (a), The geometry and representation of J_{1-3} and bond parameters of ground state $[(\text{Mn}_4\text{Cl})_3(\text{BTT})_8]^{3-}$ MOF. (Color code of Mn = red, Cl = Yellow, N = Blue, C = Grey, H = white), (b), Estimated spin-state ladder based on DFT J s for H_2 bound (red) and unbound MOF (black) (c) The spin density plot for the ground state of the $[(\text{Mn}_4\text{Cl})_3(\text{BTT})_8]^{3-}$ MOF at a cut off value of 0.005 a.u., blue color indicates alpha and red color indicates beta spin density. (d) The different interaction sites for bound hydrogen (site I, site II, site III, site IV) with respect to the optimized geometry.

as an asymmetric unit is chosen for our calculations. Our target was to understand the maximum uptake capacity for hydrogen, and therefore coordinated solvent-free environment was chosen. Although the unit cell in the asymmetric unit has a molecular formula of $[(\text{Mn}_4\text{Cl})_3(\text{BTT})_8]^{3-}$, several Mn^{2+} cations have open sites, and the coordination number is saturated upon applying periodic boundary conditions to maintain charge balance.

The binding energy (BE) for the H_2 intake was computed using the following equation:

$$E[\text{H}_2(n)] = \frac{E_T(\text{MOF.Mn.nH}_2) - E_T(\text{MOF.Mn}) - nE_T(\text{H}_2)}{n}$$

Here 'n' is the number of bound H_2 molecules, $E_T(\text{MOF.Mn.nH}_2)$ is the total energy of the hydrogen-bound MOF, $E_T(\text{MOF.Mn})$ is the total energy of the unbound MOF and $nE_T(\text{H}_2)$ is the total energy of the free H_2 molecules.

We have attempted to find possible H_2 binding pockets within the MOF, four different positions shown in Figure 1(d) as sites I to IV yielded the minimum energy structures. The binding site I was at the manganese center, where hydrogen was binding in a side-on manner at an $\text{Mn}\dots(\text{H}_2)$ distance of 2.7 Å (see Table 1). The $\text{Mn}-\text{Cl}$ and $\text{Mn}-\text{N}$ bond distances are slightly perturbed upon H_2 binding. If we compare the bound and unbound MOF geometries, it is clear that most of the structural parameters are not altered significantly, and this suggests that the MOF structure remains robust upon H_2 binding. The BE for the site I was estimated to be -15.4 kJ/mol. The second binding site is the Cl- ion (site II), where the hydrogen molecule is bound weakly to the Cl^- ion at $\text{Cl}\dots(\text{H}_2)$ distances of 3.05 and 3.54 Å. This is an asymmetric side-on binding with the $\text{Mn}-\text{H}-\text{H}$ angle of 123° , and the BE for this site is estimated to be slightly smaller (-8.5 kJ/mol). The third binding site (site III) is found to be the non-coordinated nitrogen atom of the tetrazolate ring with the H_2 found to bind in an end-on fashion with the $\text{N}\dots\text{H}-\text{H}$ distance is found to be 2.66 Å with the $\text{N}-\text{H}-\text{H}$ angle of 163° exhibiting slight bend, and this is found to bind even weaker (the BE of -7.9 kJ/mol). Site IV is identified as the carbon atom of the tetrazolate ring with the H_2 binding in a side-on fashion with the $\text{C}\dots(\text{H}_2)$ distances of 2.93 and 2.96 Å, and this site has the least binding energy (-6.3 kJ/mol).

The H_2/D_2 neutron diffraction data for this MOF is reported where the $\text{Mn}\dots\text{H}_2$ distance was estimated to be 2.27 Å, and the binding site with $\text{Cl}/\text{C}/\text{N}$ positions was also estimated to be in the range of 3.47 to 3.66 Å. (Table 1). Thus the positions/sites found here strongly correlate to the experimental neutron

diffraction data obtained at 3.5 K with H_2/D_2 loadings offering confidence in the methodology chosen. A site I have a stronger binding ability, we have also performed the binding of hydrogen for other M-BTT series ($\text{M}=\text{Cr}, \text{Fe}, \text{Cu}$) and compared their trend in binding energies (BE (in kJ/mol)) = $-16, -39, -24$, respectively) for the site I and found that the strength of interaction follows $\text{Fe} > \text{Cu} > \text{Cr} > \text{Mn}$. As Fe-BTT was found to have stronger binding than Mn, this trend is also consistent with experiments.^[81]

Going by this site binding pockets for each tetrameric model $[(\text{Mn}_4\text{Cl})_3(\text{BTT})_8]^{3-}$ there are four sites I, one site II, sixteen sites III, and eight site IV available for binding. Though the ligand BE is relatively smaller, as the available positions are larger for the ligands (twenty-four positions if we put sites III and IV together) and therefore, it has a greater uptake capacity. If the average binding energy for all four sites were computed, it turns out to be 9.6 kJ/mol per H_2 . This is strikingly correlated to the ~ 10 kJ/mol isosteric value obtained from experiments, offering confidence in the methodology chosen.^[46]

Further, we have looked at the computed Hirshfeld charges, which reveal a net positive charge on the H_2 molecule with a substantially smaller magnitude for site II–IV than the site I (Table S2). This suggests a donation of σ bonding electrons of H_2 to the bonded atoms.

The site I interaction of H_2 with the Mn^{2+} cation is found to be in the η^2 mode of binding, and hence the interaction between the metal and the H_2 molecule suggests a donation of $\sigma(\text{H}_2)$ to the d_z^2 orbital of the Mn^{2+} ion. Clearly, as Mn^{2+} is half-filled, this donation is weaker as only β -orbitals are available for acceptance.

If the d_z^2 orbital is completely vacant (such as for d^4 configuration), these may yield stronger metal... H_2 interactions. Additionally, a back donation from d_{yz} to $\sigma^*(\text{H}_2)$ though possible, we did not witness such interaction in this model.

To understand the interaction between the H_2 molecule and the binding site, AIM analysis was performed (see Figure 2). The following point emerges from this analysis (i) a bond-critical point (BCP shown as a blue dot) is visible between H_2 and the binding site atom for all sites. For sites I and IV, a symmetric η^2 - H_2 binding mode was detected, while for sites II and III, an asymmetric η^1 - H_2 was visible. (ii) In addition to the BCPs, site III also exhibits a ring critical point (RCP (3, +1)) between the N atom and the H_2 molecule. (iii) in all the sites, the core electron density is not perturbed, and only the valence shell is found to interact with the H_2 molecule (iv) for site III, the H_2 molecules are not approaching the tetrazolate ring nitrogen atom along the nitrogen lone pair, and this suggests the donation of $\sigma(\text{H}_2)$

Table 1. Selected structural parameters for various binding sites for the bound and unbound MOF, (where X = each binding site) along with neutron diffraction data reported from experiments.

parameters	Mn–Mn [Å]	Mn–Cl [Å]	Mn–Cl–Mn [°]	Mn–N [Å]	X–H ₂ [Å] (DFT)	X–H ₂ [Å] (Exp)
Unbound	3.66	2.592	89.99	2.183	–	–
Site I	3.68	2.604	89.99	2.183	2.54	2.27
Site II	3.66	2.589	89.94	2.178	3.10	3.66
Site III	3.66	2.588	89.99	2.195	2.70	3.26
Site IV	3.66	2.583	90.00	2.184	2.92	4.72

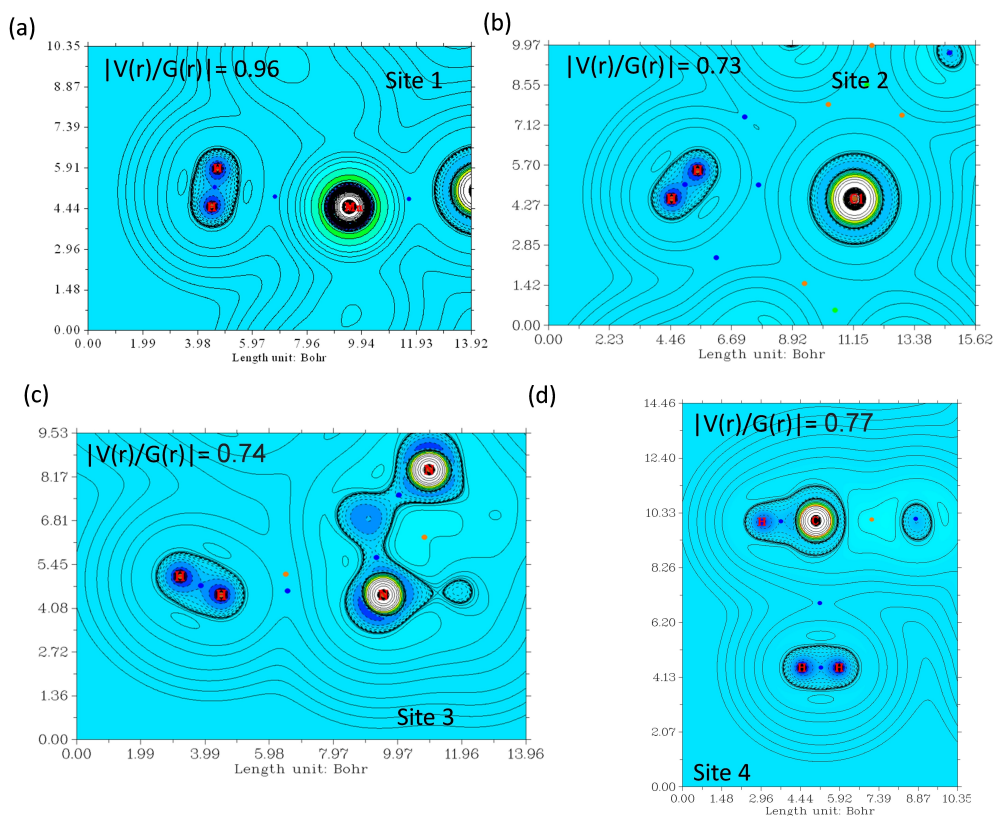


Figure 2. The AIM analysis plot for (a) site I (b) site II (c) site III (d) site IV obtained from Multiwfn software.

to the nitrogen π^* orbital and the computed charges also exemplify this point (v) the $|V(r)/G(r)|$ ratio indicates that the site...H₂ interactions are closed-shell ionic interactions, with a greater covalency detected for the site I and lesser for sites II–IV, with the strongest ionicity detected for site II.

To quantify the donor-acceptor interactions for the site I to IV, we have performed an NBO analysis. The second-order perturbation theory analysis indicates a very strong $\sigma(\text{H}_2) \rightarrow \text{Mn}(d_z^2)$ donor-acceptor interaction with a strength of 7.6 kJ/mol (Figure 3) for the site I and 5.5 kJ/mol for $\text{Cl}(\text{nb}) \rightarrow \sigma^*(\text{H}_2)$ interactions (Figure 3). The estimation of the NPA charges suggests that the bound and unbound -Cl atom charges vary by ~ 0.018 . Similar variations are also seen for the C and N atoms that lie closer to the H₂ position, rationalizing the

observed BCPs in the AIM analysis (see Table S3 in ESI). To assess and analyse the nature of BCP on expanding the basis set, we have performed calculations on a model system using def2-TZVP, def2-QZVPP and cc-PVQZ basis set approaching the complete basis set limit. Calculations on these models indicate that the $\text{Cl} \dots \text{H}_2$ interaction is intact, as revealed by the computed Laplacian values (see Table S6).

Multiple donor-acceptor interactions are found for sites III and IV, albeit with a strength of < 1 kJ/mol (see ESI Figure S1).

The total density of state reveals a significant bandgap of (~ 1.79 eV), revealing a non-metallic character of this material (see Figure S3). Further, we have analysed the partial density of the state (pdos plot) for hydrogen-bound MOF to gain insight into the bonding^[82, 83] (Figure 4). The following points emerge from this data (i) for the site I two variations are noted with the peak corresponding to the conduction band of d_z^2 orbital moving towards the Fermi level upon H₂ binding, and the corresponding valence band d_z^2 orbital getting further stabilised, affirming the bonding picture described earlier also holds valid for the periodic systems (Figure S2). Secondly, the peak corresponding to the valence band of the d_{yz} orbital shifts closer to the Fermi level, and the corresponding conduction band moves away from the Fermi level, indicating back donation of the d_{yz} orbital to $\sigma^*(\text{H}_2)$ orbital. (ii) for site II, the valence band peak corresponding to the p-orbital of the Cl ion is found to shift towards the Fermi level, affirming $\text{Cl}(\text{nb}) \rightarrow \sigma^*(\text{H}_2)$ interaction. The presence of $d_{x^2-y^2}$ orbital near the Fermi level ($E =$

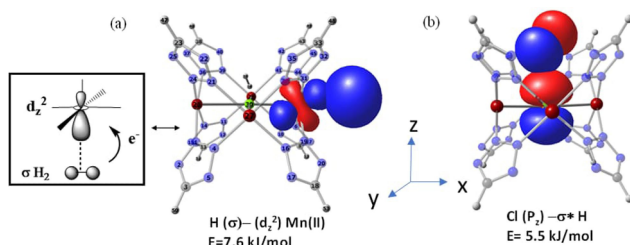


Figure 3. The Natural Bond Order analysis for the hydrogen binding at (a) Site I, (b) site II. See inset for the axis.

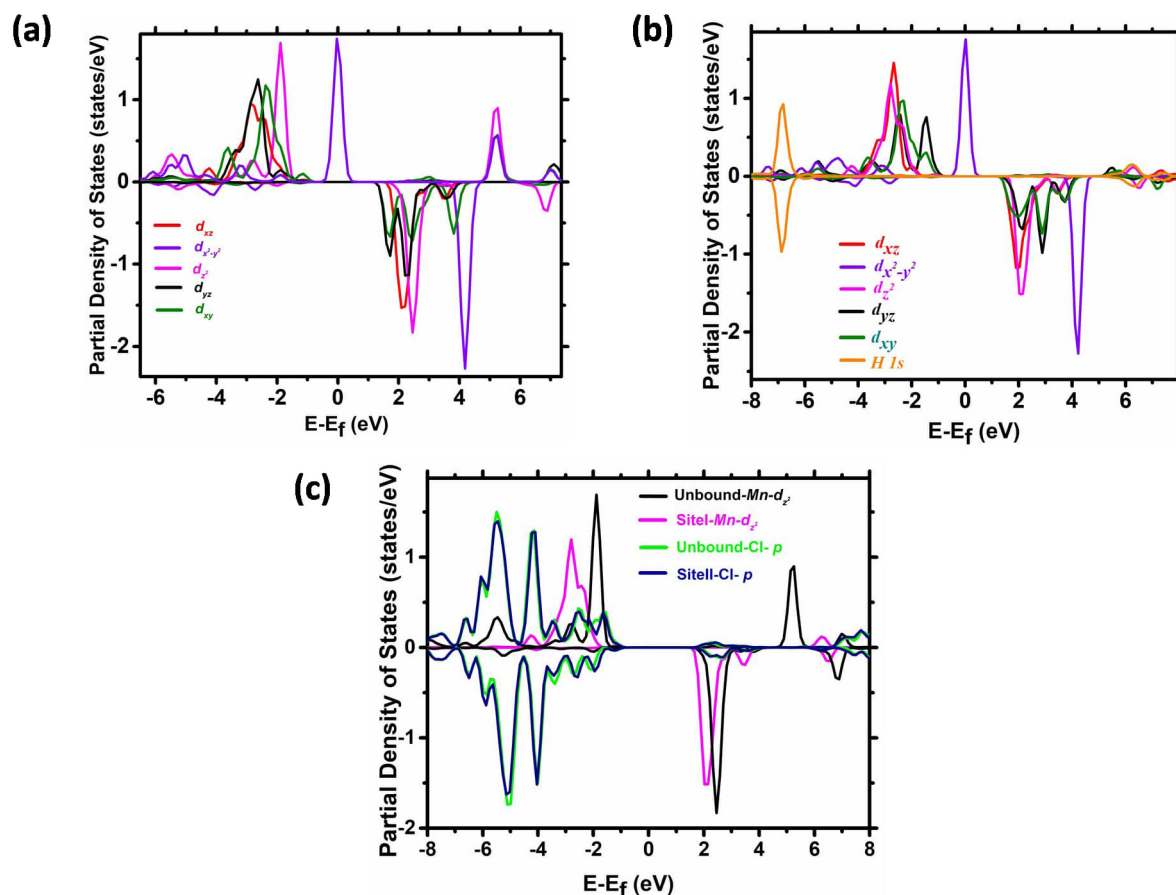


Figure 4. (a) The partial density of state for unbound MOF (b) The partial density of state for hydrogen bound MOF, where the black dotted lines indicate the Fermi energy levels. (c) The partial density of state plot for site I (Mn- d_z^2 orbital) and site II (Cl- p -orbital).

–0.15 a.u.) is also reflected in cluster model calculation employing hybrid B3LYP functional.

Experimentally neutron powder diffraction was performed to explore various binding packets with various proportions of deuterium loading.^[46] Experiments reveal a strong Mn...H₂ binding as shown in site I with the Mn...H₂ distance of 2.27 Å. These data are consistent with our calculations yielding the strongest binding energy for this site, offering confidence in the computed binding energies and the geometries. Further experiments also suggest possible binding at the –Cl site and taking up more H₂ at the ligand cavity (sites III and IV). All these experimental observations, including the number of H₂ uptake in various sites estimated from neutron data, agree with the computed results.

H₂ Uptake Capacity of Mn-BTT

The Mn-BTT MOF has been experimentally shown to have an H₂ uptake capacity of 6.9 wt% at 77 K at 90 bar pressure, with the storage density reaching up to 85% of that of liquid hydrogen. This suggests that the four sites described above have multiple H₂ uptake capacities, without which such high uptake capacity can not be reached. We have performed periodic DFT

calculations further to understand the energetic cost of such multiple H₂ binding modes and packets. We have performed calculations on six different models which combine various sites in various proportions (figure 5). Model I-I corresponds to the addition of two H₂ in two different Mn²⁺ sites. This is performed to check if there is any cooperative binding between two metal sites. The binding energy for model I-I is found to be (–14.9) kJ/mol per H₂ molecule, which is slightly lower compared to the site I binding energy (Table 1). In the next model, we have kept model I-I and added one molecule on site II (model I-I-II) or one (model I-I-III) or two (models I-I-III-III) H₂ molecules in site III, and the BE computed for these models are –13.7, –12.2 and –10.2 kJ/mol per H₂, respectively. In the next step of calculations, model I-I-III-III was taken, and an additional H₂ was added to site IV (model I-I-III-III-IV), for which the BE was estimated to be –8.6 kJ/mol per H₂ molecule, and this is smaller compared to 10.6 kJ/mol obtained if we add individual site binding energies.

The addition of another H₂ to this model (model I-I-III-III-IV with six H₂ molecules) yields BE of –8.1 kJ/mol per H₂ molecule, which is also ~2 kJ/mol lower than the individual BE computed. It is clear from this trend that the addition of further H₂ molecules is likely to yield similar BE. With six H₂ molecules, the BE tends to reach saturation, and at this point, the addition

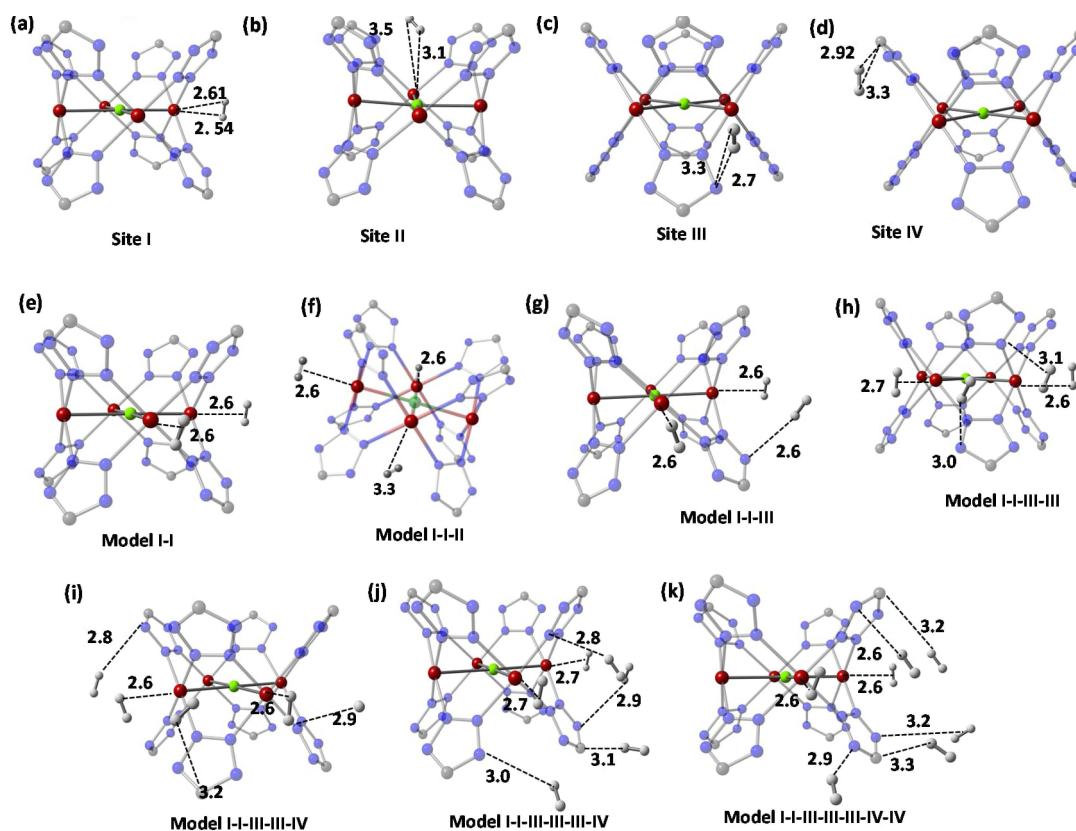


Figure 5. The interaction of hydrogen with the manganese framework for model (a) to (k), the bond distance are given in Å.

of additional H_2 is likely to be unfavourable except when the pressure is increased. We have plotted in Figure 6(a), the expected BE based on individual sites and the computed BE for various models. Up to three H_2 addition, the trend is similar, suggesting the additive nature of BE. However, further addition of H_2 molecules in sites III/IV tends to yield smaller BE than the value obtained for individual sites, suggesting a saturation level. To understand the reason behind the observed BE pattern, we have computed both interaction energy (IntE) and deformation energy (DE) by considering the binding at all sites as per the established procedure^[84] (see Table 2) (see ESI for the equations 1 and 2 used). The DE reflect the deformation in the MOF and H_2 , and when examined separately, the deformation in H_2 has amounted to less than 1 kJ/mol, and this suggests that a major part of deformation arises from the MOF part .i.e a significant portion of the deformation energy is due to deformation in the MOF geometry. Among different sites, the DE computed is found to be in the range of 23–38 kJ/mol, with sites III and IV having the maximal deformation energies.

The interaction energy accounts for chemical interactions between two deformed fragments brought from infinity to their position at the equilibrium geometry and allowed to interact (see equation S1 in ESI, Table 2). As this reflects the interaction between two fragments (MOF and H_2), this is likely to yield better insights.

The IntE for site I is -47.8 kJ/mol indicating a strong interaction between Mn^{2+} and H_2 . For site II, on the other hand,

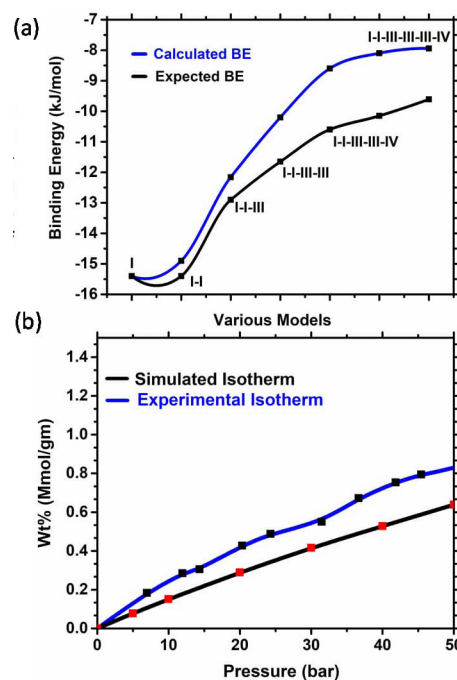


Figure 6. (a): The plot for the BE calculated vs expected for various models obtained from DFT calculation. (b) The adsorption isotherm plot for hydrogen uptake at 298 K, upto 60 bar pressure (GCMC calculations).

Table 2. DFT computed BE for individual sites/models along with the computed Interaction energy (all in kJ/mol).

Binding sites for H ₂	IntE	The Binding Energy
Site I	47.7	-15.4
Site II	32.2	-8.5
Site III	46.8	-7.9
Site IV	44.6	-6.4
Model I-I	-	-14.9
Model I-I-II	-	-13.7
Model I-I-III	-	-12.2
Model I-I-III-III	-	-10.2
Model I-I-III-III-IV	-	-8.6
Model I-I-III-III-III-IV	-	-8.1

the IntE energy dropped by 30% compared to site I (-32.2 kJ/mol), and this is due to the weaker binding of H₂ at the Cl site (See Table 2). The adsorption isotherm was simulated using GCMC simulation (Figure 6b) by incorporating the classical interactions of hydrogen employing X-ray geometry at 298 K, at a pressure range of 0–60 bar. The blue colour indicates the experimental isotherm, and the black colour, the simulated curve. Both the value as well as the trend are in line with the experiments, though the calculated data is slightly lower than the experiments.

Magnetic Exchange Interactions in Unbound MOF

This MOF has three types of exchange interactions. The J_1 denotes the interaction between adjacent manganese centers which are connected through the BTT ligand and via μ_4 -Cl bridge with the Mn–Cl–Mn angle being $< 90^\circ$. The J_2 describes the interaction between Mn centers which are connected only through a chloride bridge with the near-linear Mn–Cl–Mn angles. The J_3 interaction describes magnetic coupling among {Mn₄} tetrameric units connected by the BTT ligands (see Figure 1(a)). The computed value of J_1 is $+1.1 \text{ cm}^{-1}$, J_2 is -51 cm^{-1} , and J_3 is $+13 \text{ cm}^{-1}$, respectively, for the unbound MOF (Table 3). The J_1 interaction is ferromagnetic due to the acute Mn–Cl–Mn angles, which render the SOMOs orthogonal, leading to weak ferromagnetic coupling. Although the magnetic characterisations are not available for this MOF, the Mn(II) dimer reported with -Cl bridge having Mn–Cl–Mn angle of $< 95^\circ$ reported^[85] to have weak ferromagnetic J_s , which is consistent with our estimate offering confidence. The J_2 interaction is strongly antiferromagnetic in nature, and with near-linear Mn–Cl–Mn angles, the overlap between the SOMOs

Table 3. The comparison of exchange interaction before and after hydrogen uptake.

	J_1 [cm^{-1}]	J_2 [cm^{-1}]	J_3 [cm^{-1}]
Unbound MOF	1.1	-50.8	13.1
Site I	1.1	-51.2	13.1
Site II	1.2	-53.0	13.5
Site III	0.91	-51.4	13.1
Site IV	0.77	-51.7	13.0

is very strong, leading to strong antiferromagnetic coupling. The orbital analysis (vide infra) reveals that the d_z^2 orbital of the Mn(II) atoms lies along the -Cl ligand leading to strong head-to-head overlap and hence strong antiferromagnetic coupling. Further, Mn- d_{xz} |Cl- p_x and Mn- d_{xz} |Cl- p_y orbital were also found to have π -type interactions strengthening the antiferromagnetic J_s . This is affirmed by NBO analysis (vide infra). The J_3 interaction is also found to be ferromagnetic in nature. Though the BTT ligand's strong π electronic cloud could facilitate strong overlap, the ligands do not lie in the same plane as the tetrameric {Mn₄} cores resulting in the poor overlap between SOMOs of two {Mn₄} tetramers. Further, as this exchange is between two Mn...Mn atoms that lie far away (shortest Mn...Mn distance is 9.9 Å), McConnell type spin polarisation mechanism is visible. As an odd number of spacers present between any two Mn(II) atoms, this results in strong ferromagnetic coupling. A strong antiferromagnetic J_2 and ferromagnetic J_1 and J_3 lead to competing interactions. We have performed the phenomenological spin Hamiltonian analysis using the MAGPACK suite^[86] using the computed J values to assess and analyse various spin ladders that arise due to magnetic coupling. This yield for an {Mn₈} motif, $S=5$ as the ground state revealing strong competing interactions among the Mn(II) ions (note there are more J_3 interactions than J_2 in the network, though the latter magnitude is larger, see Figure 1(b)) with an $S=6$ and $S=4$ state close lying in energy. We have also performed MAGPACK simulation by varying the J_3 value from 13 to 51, and corresponding E/J values were plotted, which suggest that the ground state remains unaltered for the $|J_2/J_3|$ ratio in the range of 4 to 2.2 (see Figure S11). While magnetic susceptibility measurements were not performed on this particular MOF, there are several experimental studies on other Mn(II) MOFs possessing weak antiferromagnetic coupling, which is consistent with our values.^[87–89] Further, there are several studies on magnetic exchange mediated by the tetrazolate ligand similar to the connector employed here, exhibiting moderate antiferromagnetic coupling, as witnessed here.^[90] Further, the long-range ordering that is witnessed in many MOFs^[91], could be attributed to the magnetic coupling of several $S=5$ states that are expected to manifest at low temperature – thanks to the ferromagnetic J_3 interaction.

We have also explored the ground state of the system by analysing the energies of various broken symmetry configurations. The ground state of the tetrameric {Mn₄} unit is found to have one manganese spin-down and the other three Mn center spin-up, as shown in Figures 1(c) and S3. Both the computed spin-state configurations and the exchange Hamiltonian simulation with MAGPACK yield this as the ground state configuration for the given set of J values. As the H₂ bound to various sites is expected to influence the magnetic interactions, we compute the corresponding magnetic coupling with an aim to see if there are variations in the magnetic coupling before/after the gas binding. To begin with, we have calculated J_1 - J_3 for various H₂ bound models discussed above (sites I to IV, see Table 3). For all four sites, the nature of coupling remains the same, i.e. antiferromagnetic for J_2 and ferromagnetic for J_1 and J_3 . Only a minor variation in the J_s is noted as the binding of H₂

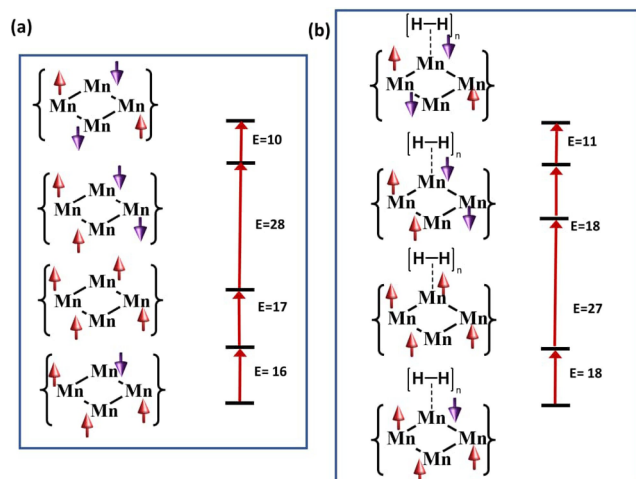


Figure 7. The energy difference between various spin configurations for (a) unbound and (b) H₂ bound Manganese center in Mn-BTT.

is very weak, and this is in contrast to our recent work on Cr(III) MOF, where O₂ binding was found to substantially alter the magnetic exchange coupling.^[18] For the site I, the J_2 interaction was found to increase slightly compared to the unbound MOF. As the Mn(II) centers move from square-pyramidal to octahedral upon H₂ binding, the overlap of the d_z^2 orbital along the Mn–Cl bond increases leading to slightly larger antiferromagnetic coupling. Although the magnitude of J_s is altered upon H₂ binding, the nature of the coupling remains the same, and therefore, the ground state configuration is the same as that of the unbound MOF, as shown in Figure 1. The J value computed for site II reveals a slightly larger J_2 , and this is due to the H₂ being bound to Cl which alters the Mn–Cl–Mn angle slightly (from 179° in unbound MOF to 175.5° in bound MOF). As the bound H₂ is far from the Mn²⁺ ions, only minor perturbations in all three J_s are noted for sites III and IV.

The energy gap of the ground-excited states is perturbed upon H₂ binding; however, the corresponding spin-state ordering remains the same (for example, the first excited state is all spin-up configuration for both bound and unbound MOF). Further, as the excited states are higher in energy by more than 15 kJ/mol, and this is much larger than the binding energy computed for each H₂ molecule, the role of excited spin-coupled states in gas binding can be neglected. (Figure 7) Further, we have calculated the binding energy of H₂ (the site I) for the high-spin state (spins are up in the Mn(II) centres), and it is found to be –15.3 kJ/mol, which is the same as the ground state suggesting that spin configurations are not altering the gas binding capacity in this MOFs. A similar analysis performed on MOF-74 also yielded a difference of 0.8 kJ/mol across various spin ladders.^[92]

Conclusions

Periodic DFT calculations were performed on [(Mn₄Cl)₃(BTT)₈]³⁻ the metal-organic framework to assess and understand various

H₂ binding pockets and the nature of the interaction between the gas and the MOF architecture. Further, as the Mn(II) ions are bridged by –Cl and the benzene tris tetrazolate ligand, strong exchange interaction was expected. Our calculations suggest there are three different exchange interactions present in this MOF, which were estimated to be ferro or antiferromagnetic leading to a three-up-one-down spin configuration for each {Mn₄} tetrameric unit resulting in an $S=5$ state which is found to be weakly ferromagnetically coupled to other tetrameric units in the MOF network. Our calculations suggest four H₂ binding sites I to IV, with the strongest binding detected at the metal site with the Mn²⁺...H₂ in η^2 mode of binding with the distance of 2.27 Å and binding energy of –15.4 kJ/mol. The bonding analysis performed using NBO and AIM analysis reveal a donation of σ (H₂) to the d_z^2 orbital of the Mn²⁺ ion. The binding of H₂ at the –Cl (site II) and other ligand packets (site III and IV) were found to have favourable binding, with the computed binding energy decreasing in the following order I > II > III > IV, which was also validated by the interaction energy calculations. The average binding energy computed for these four sites was found to strikingly match the experimental isosteric value (9.5 kJ/mol vs ~10 kJ/mol). For sites II and III, an asymmetric η^1 -H₂ binding with –Cl and –N atoms was detected and in all cases, AIM analysis indicated a bond-critical point affirming stronger interactions. The Mn...H₂ interaction is found to have strong covalency, and significantly less covalency is found for other sites. Various models were explored for multiple H₂ uptakes, and these calculations suggest that the computed binding energy is additive up to the uptake of three H₂, beyond which it decreases. This implies that the addition of H₂ at various sites simultaneously reduces the overall per-site binding energy leading to saturation. Here both electronic and steric factors are expected to play a role. The magnetic exchange computed upon binding yields only minor alteration in the J_s , which reveals that spin-state and exchange-coupled state are unlikely to play a role in the H₂ uptake/storage, which is in stark contrast to O₂ binding in Cr-MOF reported.

Acknowledgements

We thank DST and SERB (DST/SJF/CSA-03/2018-10; SB/SJF/2019-20/12). RJ thanks DST-INSPIRE for a fellowship.

Conflict of Interest

There are no conflicts to declare.

Keywords: density functional calculations • exchange coupling • gas adsorption • MOFs • spin-states calculations

[1] S. Ou, C.-D. Wu, *Inorg. Chem. Front.* **2014**, *1*, 721–734.

[2] J. Gascon, A. Corma, F. Kapteijn, F. X. Llabres i Xamena, *ACS Catal.* **2014**, *4*, 361–378.

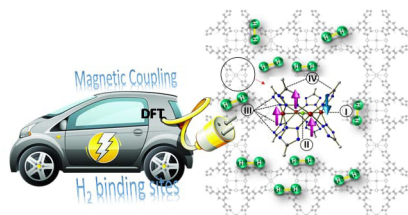
- [3] N. Huang, H. Drake, J. Li, J. Pang, Y. Wang, S. Yuan, Q. Wang, P. Cai, J. Qin, H. C. Zhou, *Angew. Chem. Int. Ed.* **2018**, *130*, 9054–9058.
- [4] W.-G. Cui, G.-Y. Zhang, T.-L. Hu, X.-H. Bu, *Coord. Chem. Rev.* **2019**, *387*, 79–120.
- [5] J. S. Lee, E. A. Kapustin, X. Pei, S. Llopis, O. M. Yaghi, F. D. Toste, *Chem.* **2020**, *6*, 142–152.
- [6] H. Xu, F. Liu, Y. Cui, B. Chen, G. Qian, *Chem. Commun.* **2011**, *47*, 3153–3155.
- [7] Z.-Z. Lu, R. Zhang, Y.-Z. Li, Z.-J. Guo, H.-G. Zheng, *J. Am. Chem. Soc.* **2011**, *133*, 4172–4174.
- [8] C. Zhang, L. Sun, Y. Yan, J. Li, X. Song, Y. Liu, Z. Liang, *Dalton Trans.* **2015**, *44*, 230–236.
- [9] Z. Guo, X. Song, H. Lei, H. Wang, S. Su, H. Xu, G. Qian, H. Zhang, B. Chen, *Chem. Commun.* **2015**, *51*, 376–379.
- [10] J. Wang, M. Jiang, L. Yan, R. Peng, M. Huangfu, X. Guo, Y. Li, P. Wu, *Inorg. Chem.* **2016**, *55*, 12660–12668.
- [11] P. Horcajada, T. Chalati, C. Serre, B. Gillet, C. Sebrie, T. Baati, J. F. Eubank, D. Heurtaux, P. Clayette, C. Kreuz, *Nat. Mater.* **2010**, *9*, 172–178.
- [12] H.-N. Wang, X. Meng, G.-S. Yang, X.-L. Wang, K.-Z. Shao, Z.-M. Su, C.-G. Wang, *Chem. Commun.* **2011**, *47*, 7128–7130.
- [13] J. Zhuang, C.-H. Kuo, L.-Y. Chou, D.-Y. Liu, E. Weerapana, C.-K. Tsung, *ACS Nano* **2014**, *8*, 2812–2819.
- [14] W. Cai, J. Wang, C. Chu, W. Chen, C. Wu, G. Liu, *Adv. Sci.* **2019**, *6*, 1801526.
- [15] M. X. Wu, Y. W. Yang, *Adv. Mater.* **2017**, *29*, 1606134.
- [16] J. Wu, J.-W. Xu, W.-C. Liu, S.-Z. Yang, M.-M. Luo, Y.-Y. Han, J.-Q. Liu, S. R. Batten, *Inorg. Chem. Commun.* **2016**, *71*, 32–34.
- [17] P. Horcajada, C. Serre, M. Vallet-Regí, M. Sebban, F. Taulelle, G. Férey, *Angew. Chem. Int. Ed.* **2006**, *118*, 6120–6124.
- [18] E. D. Bloch, W. L. Queen, M. R. Hudson, J. A. Mason, D. J. Xiao, L. J. Murray, R. Flacau, C. M. Brown, J. R. Long, *Angew. Chem. Int. Ed.* **2016**, *128*, 8747–8751.
- [19] E. D. Bloch, W. L. Queen, R. Krishna, J. M. Zadrozny, C. M. Brown, J. R. Long, *Science* **2012**, *335*, 1606–1610.
- [20] D. A. Reed, D. J. Xiao, M. I. Gonzalez, L. E. Darago, Z. R. Herm, F. Grandjean, J. R. Long, *J. Am. Chem. Soc.* **2016**, *138*, 5594–5602.
- [21] E. D. Bloch, L. J. Murray, W. L. Queen, S. Chavan, S. N. Maximoff, J. P. Bigi, R. Krishna, V. K. Peterson, F. Grandjean, G. J. Long, *J. Am. Chem. Soc.* **2011**, *133*, 14814–14822.
- [22] J. Cui, Y. Li, Z. Guo, H. Zheng, *Chem. Commun.* **2013**, *49*, 555–557.
- [23] G. R. Lorzing, B. A. Trump, C. M. Brown, E. D. Bloch, *Chem. Mater.* **2017**, *29*, 8583–8587.
- [24] B. Wang, R.-B. Lin, Z. Zhang, S. Xiang, B. Chen, *J. Am. Chem. Soc.* **2020**, *142*, 14399–14416.
- [25] S. Xiang, W. Zhou, J. M. Gallegos, Y. Liu, B. Chen, *J. Am. Chem. Soc.* **2009**, *131*, 12415–12419.
- [26] J. Jiang, H. Furukawa, Y.-B. Zhang, O. M. Yaghi, *J. Am. Chem. Soc.* **2016**, *138*, 10244–10251.
- [27] E. Tsvion, J. R. Long, M. Head-Gordon, *J. Am. Chem. Soc.* **2014**, *136*, 17827–17835.
- [28] L. Ma, D. J. Mihalczik, W. Lin, *J. Am. Chem. Soc.* **2009**, *131*, 4610–4612.
- [29] Y. He, W. Zhou, G. Qian, B. Chen, *Chem. Soc. Rev.* **2014**, *43*, 5657–5678.
- [30] H. Zhang, P. Deria, O. K. Farha, J. T. Hupp, R. Q. Snurr, *Energy Environ. Sci.* **2015**, *8*, 1501–1510.
- [31] Y. Li, R. T. Yang, *J. Am. Chem. Soc.* **2006**, *128*, 726–727.
- [32] D. Denysenko, M. Grzywa, M. Tonigold, B. Streppel, I. Krkljus, M. Hirscher, E. Mugnaioli, U. Kolb, J. Hanss, D. Volkmer, *Chem. Eur. J.* **2011**, *17*, 1837–1848.
- [33] H. Park, J. F. Britten, U. Mueller, J. Lee, J. Li, J. B. Parise, *Chem. Mater.* **2007**, *19*, 1302–1308.
- [34] K. Prasanth, P. Rallapalli, M. C. Raj, H. Bajaj, R. V. Jasra, *Int. J. Hydrogen Energy* **2011**, *36*, 7594–7601.
- [35] G. Feng, Y. Peng, W. Liu, F. Chang, Y. Dai, W. Huang, *Inorg. Chem.* **2017**, *56*, 2363–2366.
- [36] B. M. Connolly, D. G. Madden, A. E. Wheatley, D. Fairen-Jimenez, *J. Am. Chem. Soc.* **2020**, *142*, 8541–8549.
- [37] H. Bunzen, F. Kolbe, A. Kalytta-Mewes, G. Sastre, E. Brunner, D. Volkmer, *J. Am. Chem. Soc.* **2018**, *140*, 10191–10197.
- [38] M. T. Kapelowski, S. J. Geier, M. R. Hudson, D. Stück, J. A. Mason, J. N. Nelson, D. J. Xiao, Z. Hulvey, E. Gilmour, S. A. FitzGerald, *J. Am. Chem. Soc.* **2014**, *136*, 12119–12129.
- [39] M. Dinca, A. F. Yu, J. R. Long, *J. Am. Chem. Soc.* **2006**, *128*, 8904–8913.
- [40] R. Freund, O. Zaremba, G. Arnauts, R. Ameloot, G. Skorupskii, M. Dincă, A. Bavykina, J. Gascon, A. Ejsmont, J. Goscińska, *Angew. Chem. Int. Ed.* **2021**, *60*, 23975–24001.
- [41] J.-R. Jiménez, A. Sugahara, M. Okubo, A. Yamada, L.-M. Chamoreau, L. Lisnard, R. Lescouëzec, *Chem. Commun.* **2018**, *54*, 5189–5192.
- [42] F. Tan, A. López-Periágo, M. E. Light, J. Cirera, E. Ruiz, A. Borrás, F. Teixidor, C. Viñas, C. Domingo, J. G. Planas, *Adv. Mater.* **2018**, *30*, 1800726.
- [43] H. Liang, X. Jiao, C. Li, D. Chen, *J. Mater. Chem. A* **2018**, *6*, 334–341.
- [44] G. M. Espallargas, E. Coronado, *Chem. Soc. Rev.* **2018**, *47*, 533–557.
- [45] C. Healy, K. M. Patil, B. H. Wilson, L. Hermanspahn, N. C. Harvey-Reid, B. I. Howard, C. Kleinjan, J. Kolien, F. Payet, S. G. Telfer, *Coord. Chem. Rev.* **2020**, *419*, 213388.
- [46] M. Dinca, A. Dailly, Y. Liu, C. M. Brown, D. A. Neumann, J. R. Long, *J. Am. Chem. Soc.* **2006**, *128*, 16876–16883.
- [47] D. J. Xiao, M. I. Gonzalez, L. E. Darago, K. D. Vogiatzis, E. Haldoupis, L. Gagliardi, J. R. Long, *J. Am. Chem. Soc.* **2016**, *138*, 7161–7170.
- [48] D. A. Reed, D. J. Xiao, H. Z. Jiang, K. Chakarawet, J. Oktawiec, J. R. Long, *Chem. Sci.* **2020**, *11*, 1698–1702.
- [49] V. Colombo, G. Galli, H. J. Choi, G. D. Han, A. Maspero, G. Palmisano, N. Masciocchi, J. R. Long, *Chem. Sci.* **2011**, *2*, 1311–1319.
- [50] M. Dinca, J. R. Long, *J. Am. Chem. Soc.* **2007**, *129*, 11172–11176.
- [51] A. Kuc, T. Heine, G. Seifert, H. A. Duarte, *Chem. Eur. J.* **2008**, *14*, 6597–6600.
- [52] K. Sillar, A. Hofmann, J. Sauer, *J. Am. Chem. Soc.* **2009**, *131*, 4143–4150.
- [53] M. M. Deshmukh, M. Ohba, S. Kitagawa, S. Sakaki, *J. Am. Chem. Soc.* **2013**, *135*, 4840–4849.
- [54] F. R. Rehak, G. Piccini, M. Alessio, J. Sauer, *Phys. Chem. Chem. Phys.* **2020**, *22*, 7577–7585.
- [55] J.-J. Zheng, S. Kusaka, R. Matsuda, S. Kitagawa, S. Sakaki, *J. Am. Chem. Soc.* **2018**, *140*, 13958–13969.
- [56] L. Valenzano, B. Civalieri, K. Sillar, J. Sauer, *J. Phys. Chem. C* **2011**, *115*, 21777–21784.
- [57] R. Nabi, G. Rajaraman, *Chem. Commun.* **2019**, *55*, 8238–8241.
- [58] R. Jose, S. Kancharlapalli, T. K. Ghanty, S. Pal, G. Rajaraman, *Chem. Eur. J.* **2022**.
- [59] E. Ruiz, S. Alvarez, J. Cano, V. Polo, *J. Chem. Phys.* **2005**, *123*, 164110.
- [60] B. Zhang, Y. Duan, K. Johnson, *J. Chem. Phys.* **2012**, *136*, 064516.
- [61] I. Choudhuri, D. G. Truhlar, *Molecules* **2020**, *25*, 1552.
- [62] P. Comba, S. Hausberg, B. Martin, *J. Phys. Chem. A* **2009**, *113*, 6751–6755.
- [63] E. Ruiz, J. Cano, S. Alvarez, P. Alemany, *J. Comput. Chem.* **1999**, *20*, 1391–1400.
- [64] H. Schurkus, D.-T. Chen, H.-P. Cheng, G. Chan, J. Stanton, *J. Chem. Phys.* **2020**, *152*, 234115.
- [65] J. J. Goings, S. M. Ohlsen, K. M. Blaisdell, D. P. Schofield, *J. Phys. Chem. A* **2014**, *118*, 7411–7417.
- [66] A. Kuc, T. Heine, G. Seifert, H. A. Duarte, *Chem. Eur. J.* **2008**, *14*, 6597–6600.
- [67] R. M. Kumar, V. Subramanian, *Int. J. Hydrogen Energy* **2011**, *36*, 10737–10747.
- [68] M. K. Agusta, A. G. Saputro, V. V. Tanuwijaya, N. N. Hidayat, H. K. Dipojono, *Procedia Eng.* **2017**, *170*, 136–140.
- [69] S. Kancharlapalli, A. Gopalan, M. Haranczyk, R. Q. Snurr, *J. Chem. Theory Comput.* **2021**, *17*, 3052–3064.
- [70] H. Chen, R. Q. Snurr, *J. Phys. Chem. C* **2021**, *125*, 21701–21708.
- [71] D. Dubbeldam, S. Calero, D. E. Ellis, R. Q. Snurr, *Mol. Simul.* **2016**, *42*, 81–101.
- [72] J. Heinen, D. Dubbeldam, *Wiley Interdiscip. Rev.: Comput. Mol. Sci.* **2018**, *8*, e1363.
- [73] D. Dubbeldam, K. S. Walton, T. J. Vlugt, S. Calero, *Adv. Theory Simul.* **2019**, *2*, 1900135.
- [74] J. J. Potoff, J. I. Siepmann, *AIChE J.* **2001**, *47*, 1676–1682.
- [75] J. P. Mota, D. Martins, D. Lopes, I. Catarino, G. G. Bonfait, *J. Phys. Chem. C* **2017**, *121*, 24252–24263.
- [76] J. Jiang, *AIChE J.* **2009**, *55*, 2422–2432.
- [77] J. G. McDaniel, S. Li, E. Tylianakis, R. Q. Snurr, J. Schmidt, *J. Phys. Chem. C* **2015**, *119*, 3143–3152.
- [78] M. Fischer, B. Kuchta, L. Firlje, F. Hoffmann, M. Fröba, *J. Phys. Chem. C* **2010**, *114*, 19116–19126.
- [79] J. Camp, V. Stavila, M. D. Allendorf, D. Prendergast, M. Haranczyk, *J. Phys. Chem. C* **2018**, *122*, 18957–18967.
- [80] D. J. Xiao, M. I. Gonzalez, L. E. Darago, K. D. Vogiatzis, E. Haldoupis, L. Gagliardi, J. R. Long, *J. Am. Chem. Soc.* **2016**, *138*, 7161–7170.
- [81] K. Sumida, S. Horike, S. S. Kaye, Z. R. Herm, W. L. Queen, C. M. Brown, F. Grandjean, G. J. Long, A. Dailly, J. R. Long, *Chem. Sci.* **2010**, *1*, 184–191.
- [82] J. Wang, D. Zhou, G.-L. Wang, L. Lu, Y. Pan, A. Singh, A. Kumar, *Inorg. Chim. Acta* **2019**, *492*, 186–191.

- [83] M. Zhang, K. Gu, X. Huang, Y. Chen, *Phys. Chem. Chem. Phys.* **2019**, *21*, 19226–19233.
- [84] Q. Sun, T. Berkelbach, N. Blunt, G. Booth, S. Guo, Z. Li, J. Liu, J. McClain, E. Sayfutyarova, S. Sharma, *arXiv preprint arXiv:1701.08223*.
- [85] J.-Z. Wu, E. Bouwman, A. M. Mills, A. L. Spek, J. Reedijk, *Inorg. Chim. Acta* **2004**, *357*, 2694–2702.
- [86] J. Borrás-Almenar, J. Clemente-Juan, E. Coronado, B. Tsukerblat, *Inorg. Chem.* **1999**, *38*, 6081–6088.
- [87] Y. Li, W.-Q. Zou, M.-F. Wu, J.-D. Lin, F.-K. Zheng, Z.-F. Liu, S.-H. Wang, G.-C. Guo, J.-S. Huang, *CrystEngComm*. **2011**, *13*, 3868–3877.
- [88] S. S. Dhankhar, C. Nagaraja, *RSC Adv.* **2016**, *6*, 86468–86476.
- [89] Z.-B. Han, R.-Y. Lu, Y.-F. Liang, Y.-L. Zhou, Q. Chen, M.-H. Zeng, *Inorg. Chem.* **2012**, *51*, 674–679.
- [90] A. J. Mota, A. Rodríguez-Diéguez, M. A. Palacios, J. M. Herrera, D. Luneau, E. Colacio, *Inorg. Chem.* **2010**, *49*, 8986–8996.
- [91] L. Shen, S.-W. Yang, S. Xiang, T. Liu, B. Zhao, M.-F. Ng, J. Göettlicher, J. Yi, S. Li, L. Wang, J. Ding, B. Chen, S.-H. Wei, Y. P. Feng, *J. Am. Chem. Soc.* **2012**, *134*, 17286–17290.
- [92] A. de Oliveira, G. F. de Lima, H. A. De Abreu, *Chem. Phys. Lett.* **2018**, *691*, 283–290.
- [93] T. Lu, F. Chen, *J. Comput. Chem.* **2012**, *33*, 580–592

Manuscript received: April 14, 2022
Revised manuscript received: November 3, 2022
Accepted manuscript online: November 4, 2022
Version of record online: ■■■, ■■■■

RESEARCH ARTICLE

Origin of the large hydrogen uptake capacity of Mn(II)-based $[(\text{Mn}_4\text{Cl})_3(\text{BTT})_8]^{3-}$ ($\text{BTT}^{3-} = 1,3,5$ -benzenetristetrazolate) metal-organic framework is studied using periodic density functional theory calculations. The calculations show that there are many strong binding pockets available for hydrogen to bind, thus enhancing the uptake capacity.



R. Jose, Prof. S. Pal, Prof. G. Rajaraman**

1 – 12

A Theoretical Perspective to Decipher the Origin of High Hydrogen Storage Capacity in Mn(II) Metal-Organic Framework

